Materials Science & Engineering A 848 (2022) 143399

Contents lists available at ScienceDirect

Materials Science & Engineering A

journal homepage: www.elsevier.com/locate/msea

High thermal stability of nanocrystalline $FeNi_2CoMo_{0.2}V_{0.5}$ high-entropy alloy by twin boundary and sluggish diffusion

N.N. Liang [1], R.R. Xu [1], G.Z. Wu, X.Z. Gao, Y.H. Zhao [*]

Nano and Heterogeneous Materials Center, School of Materials Science and Engineering, Nanjing University of Science and Technology, Nanjing, 210094, China

ARTICLE INFO

Keywords:
High entropy alloy
High pressure torsion
Thermal stability
Deformation twins
Sluggish diffusion

ABSTRACT

A nanocrystalline (NC) face-centered cubic FeNi2CoMo0.2V0.5 high-entropy alloy was produced by high pressure torsion (HPT). The evolutions of microhardness and microstructure of the NC alloy during subsequent isochronal annealing were investigated systematically by electron back-scattering diffraction (EBSD) and high-resolution transmission electron microscopy (HRTEM). It was found that nano-grains and deformation nano-twin lamella were obtained at outer disk edge after HPT process with a hardness plateau of 450 HV. Isochronal annealing below 600 °C induced an evident hardening without precipitation effect, due to the annihilation of mobile dislocations and sustained deformation twin barriers. Evident recrystallization and grain growth of the NC FeNi2CoMo0.2V0.5 high-entropy alloy occurred during isochronal annealing at temperatures higher than 600 °C. The activation energies of recrystallization and grain growth of the NC FeNi2CoMo0.2V0.5 high-entropy alloy were calculated to be 350 kJ/mol and 272 kJ/mol, respectively, corresponding to a slow defects recovery process and a swift GB migration process. The high thermal stability of the NC FeNi2CoMo0.2V0.5 high-entropy was mainly caused by kinetic sluggish diffusion effect and deformation twin boundaries with thermodynamic low boundary energy, which retarded the movements of dislocations and grain boundary.

1. Introduction

In the past 40 years, it has been found that the high strength of nanocrystalline (NC) metals and alloys is always accompanied by low thermal stability. This is the so-called strength-thermal stability trade-off paradox, which seriously affects the application of NC metals in high-temperature field [1–3]. The low thermal stability of NC materials is caused by their high fraction of grain boundaries (GBs) where the atomic packing is less dense and more disordered. As a result, the configurational and vibrational entropy as well as Gibbs energy of the entire system are increased [4]. In order to improve the thermal stability, alloying elements were usually introduced into pure NC metals to lower the grain growth kinetics and thermodynamic driving force [5–8].

During the last decade, high entropy alloys (HEAs) composed of five or more major elemental species have attracted immense attentions by their exceptional mechanical properties and thermal stability [9–12]. The HEAs are found to have four core effects: thermodynamic high entropy effect, kinetic sluggish diffusion effect, atomic lattice distortion effect, and property cocktail effect [13,14]. Specially, sluggish diffusion and high entropy effect were reported to be beneficial for thermal stability [15–19]. Zhao et al. [19] revealed that coarsening of $L1_2$ precipitates in $(NiCoFeCr)_{94}Ti_2Al_4$ HEA was much slower than that in the conventional Ni-based alloys. The retardant process was owing to sluggish diffusion which slows down the diffusion kinetics. Zhou et al. [15] summarized the mechanisms of sluggish diffusion effect on thermal stability in three ways: (i) local sites with a wider distribution of metastable energy levels, (ii) the slowest diffusion rates of segregating element and (iii) Zener pinning. As for high-entropy effects, GB high-entropy effects were demonstrated via significantly decreasing GB energy with increasing temperature, thereby reducing the thermodynamic driving force for grain growth [15–17]. Refractory HEAs, as a category of emerging multi-component elements and showing superior mechanical properties at elevated temperatures [20–22], have been reported to have comparatively high thermal stability. This is because those refractory elements such as Nb, Mo, and Ta, have higher melting points than the 3d transition metal constituents. Then the diffusion kinetics may slow down within the material [10]. To illustrate, Zou et al. [22] found that NC-NbMoTaW micro-pillars annealed at 1100 °C for 72

* Corresponding author.
E-mail address: yhzhao@njust.edu.cn (Y.H. Zhao).
[1] Equal contributions.

https://doi.org/10.1016/j.msea.2022.143399
Received 3 December 2021; Received in revised form 29 April 2022; Accepted 31 May 2022
Available online 2 June 2022

h experience no noticeable change in their initial grain size of 70–100 nm and yield strength of 5 GPa. However, most of these refractory elements are rare earth elements and expensive which limits their applications.

Except the above alloying strategy to stabilize the NC grains, twin boundaries (TBs) and low-angle GBs with low energy can also be utilized to enhance thermal stability of NC metals [1,3,23–28]. Zhang et al. [23] reported that NC 330 stainless-steel films with nanoscale growth twins also exhibit better thermal stability than monolithic nanocrystals with high-angle GBs. Saldana et al. [24,27] introduced high-density coherent nanotwins into NC Cu by severe plastic deformation (SPD) at cryogenic temperatures. As a result, the thermal stability was markedly improved due to TBs pinning effect to grain and subgrain structures. As for HEAs, rare research focused on the effect of twins on the thermal stability apart from the above four core effects. Therefore, the thermal stability of NC HEAs with different grain architectures needs to be quantitatively and theoretically addressed.

In the present work, we systematically studied the thermal stability of NC FeNi2CoMo0.2V0.5 HEA processed by high pressure torsion (HPT). Both structural and kinetic factors as well as the effect of element diffusion on thermal stability are considered in the experiments.

2. Experimental procedures

To synthesize the FeNi2CoMo0.2V0.5 HEA, high-purity elements (at least 99.9 wt%) were arc melted and drop cast into cylindrical copper molds with 30 mm in diameter and 70 mm in length under pure Ar atmosphere. The drop cast ingots were encapsulated, evacuated in quartz ampules and homogenized for 72 h at 1600 °C. Details of the melting and casting process can be found elsewhere [29]. The initial homogenized grain size is about 200 μm. For the HPT process (Fig. 1a), disks with a diameter of 20 mm and a thickness of 1.5 mm were cut from the homogenized ingot by electrical discharge machining. The HPT process was conducted at room temperature at a nominal pressure of 5 GPa and a speed of 1 rotation per minute. Six rotations were employed with an equivalent strain of 5.6 at outer edge region of the disk.

Thermal stability of the HPT deformed FeNi2CoMo0.2V0.5 HEA samples was examined by isothermal heat treatments at 400 °C, 600 °C, 700 °C and 800 °C for 1h. Vickers micro-hardness measurements were conducted on a microhardness tester using a load of 2.94 N and a loading time of 15 s. Each micro-hardness value was averaged from four tested data. Micro-hardness along the radius from the disk center to edge was finally obtained. The standard deviations from averaged data were used as an indicator of the error.

The microstructure and element distribution of the HPT deformed and annealed samples were characterized by electron backscattered diffraction (EBSD) and energy dispersive spectrometer (EDS) techniques. Samples were cut from the disk plane perpendicular to the longitudinal HPT pressure direction (Fig. 1b). Then samples were ground and electro-polished using 20 V alternating current in 10% $HClO_4$ and 90% CH_3COOH at room temperature. Scanning was completed using Zeiss Auriga crossbeam microscope operated at 5 kV and equipped Oxford EBSD and EDS detector working at 20 kV. The step size for EBSD detecting is 0.01 μm. Standard bright-field images and diffraction patterns were obtained by a TECNAI 20 LaB6 transmission electron microscope (TEM) operating at 200 kV. TEM specimens were prepared by first mechanically grinding the samples to a thickness of about 45 μm, then conventional electro-polishing methods were employed in a solution containing 30% $HClO_4$ and 70% CH_3CH_2OH at −30 °C. X-ray diffraction (XRD) was performed to identify the phases in the material using Cu-Kα_1 at 40 kV and 40 mA.

3. Results

3.1. Hardness and microstructures of HPT processed sample

Fig. 2 presents the microhardness evolution along the HPT deformed disk radius and the microhardness of the homogenized sample before the HPT process. The initial sample has a hardness of about 160 HV. After 6 rotations HPT, the hardness sharply increased to 275 HV in the disk center, due to SPD-induced grain refinement and strain hardening. As the test point moves away from the disk center, microhardness value increases progressively and reached a maximum value of about 480 HV when the distance to disk center is about 3.5 mm. Then the microhardness keeps nearly unchanged and forms a broad plateau till to the outer edge of the disk. The hardness discrepancy is related to the degree of deformation which has a linear relationship with the disk radius [12,30]. The broad microhardness plateau was caused by the dynamic balance between grain refinement and recovery. Therefore, one can conclude the microstructure is uniform within the plateau. So, billets cut

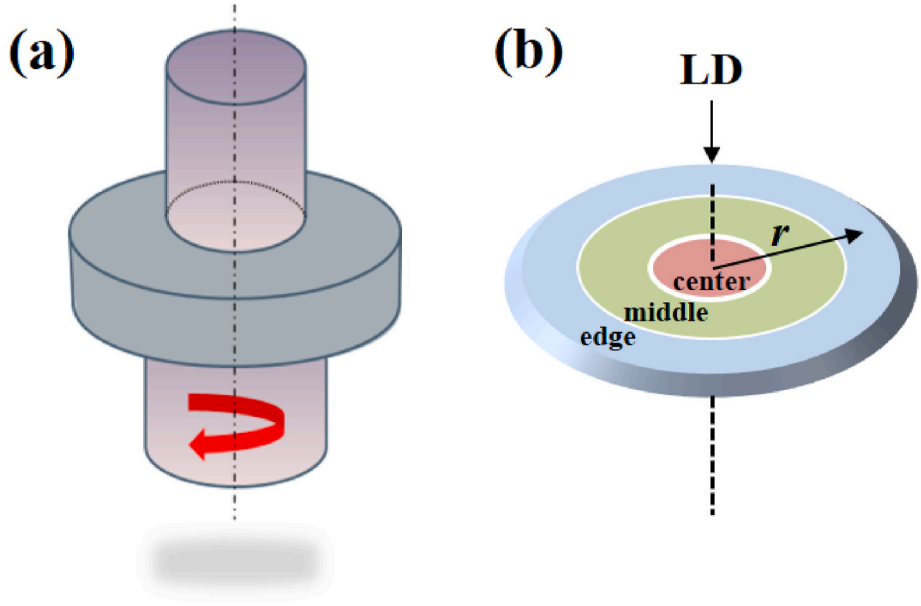

Fig. 1. Schematic representations of HPT device (a) and sample disk (b) with radius r and loading direction (LD). Center, middle from center to edge and edge were identified for following TEM and annealing process.

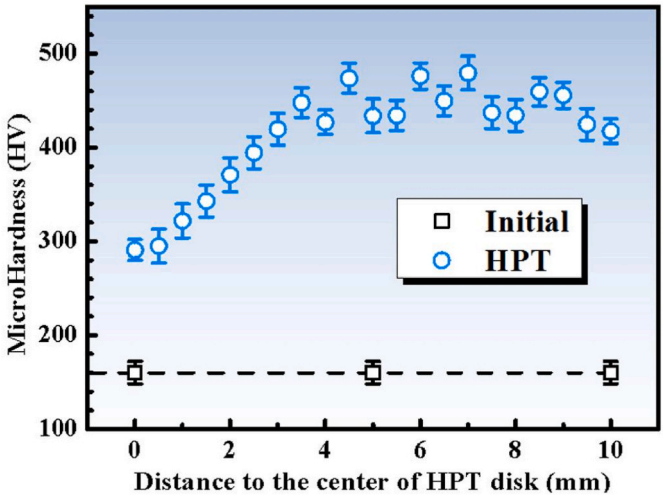

Fig. 2. Microhardness variation along the radius of the HPT disks.

only from the plateau were used for the subsequent annealing process. The plateau in hardness, with an average value of about 450 HV [31,32], indicates a saturation in grain refinement. Furthermore, the fluctuation in hardness plateau with large error bars indicates unevenness in grain refinement.

Fig. 3 displays the EDS and EBSD results of the HPT processed FeNi2CoMo0.2V0.5 HEA. As shown in Fig. 3a, uniform distribution of constituent elements is detected indicating the inexistence of element segregation during SPD process. Initial coarse grains (CGs) were deformed and severely refined by HPT as shown in Fig. 3b and c. Irregular and equiaxed small grains with non-uniform distribution were formed. The grains with random orientations are surrounded by high angle GBs, while some low angle GBs are also observed. Moreover, the interiors of grains are relatively clean, possibly due to the combined effects of dynamic recovery and recrystallization during HPT process [33]. GB misorientation distribution map is exhibited in Fig. 3d and exhibits a bimodal distribution with one peak appearing at low angles and the other peak at high angles. The fraction of low angle GBs is 54%. Grain size distribution ranging from tens to hundreds of nanometers is shown in Fig. 3e. The average grain size is 54 nm and most grains are lie in nano-scale [32,34].

Bright-filed TEM images taken from the disk edge is presented in Fig. 4. As shown in Fig. 4a, the microstructure was eventually transformed into uniform NC grains [31,32,35]. Continuous ring-like Debye-Scherer selected area electron diffraction (SAED) pattern of the inset in Fig. 4a indicates random oriented NC grains. Massive elongated grains with clear GBs (pointed out by black arrows) are homogeneously mixed with dislocation cells (pointed out by white arrows) in Fig. 4b and c. The HRTEM images in Fig. 5a and b displays a clear high angle GB (marked by the white dotted line), and a paradigmatic 14° low angle GB (marked by the red dotted line) formed by accumulation of high-density dislocations (marked by white "⊥"). In addition, some grains contain high-density deformation twins as marked by the red arrows and "T" in Fig. 4b and c, which was further proved as twin lamellae in Fig. 4d. As shown in Fig. 5c and d, the typical [110] Z.A. HRTEM images of the NC FeNi2CoMo0.2V0.5 HEA, high-density SFs on two {111} slip systems intersect in a grain and consecutive nano-scale twin lamellae with rough TBs divide the grain matrix, accompanying with massive SFs at TBs. The above results indicate a multiple grain refinement mechanism in the HPT-processed FeNi2CoMo0.2V0.5 HEA, including dislocation subdivision, SFs intersection and twinning segmentation.

Blurry structures with ill-defined boundaries are observed in Fig. 4b and c, owing to internal stresses or strains related to the non-equilibrium GBs in SPD-produced materials [33,36]. The SAED pattern shows Debye rings with a sequence that is consistent with a single-phase fcc structure for the SPD-produced HEA. The relatively early onset of twinning here is related to the low stacking fault energy of FeNi2CoMo0.2V0.5 HEA and HPT-induced severely plastic strains [11,37–39]. Deformation twins were frequently observed in materials with low stacking fault energy, such as CuZn alloys [30,40,41]. Similar observations were made in austenitic steels [42], Mg alloy [43] and FeCoCrNi HEA [44].

3.2. Hardness and microstructure evolutions during annealing

Fig. 6 shows the microhardness evolution during annealing

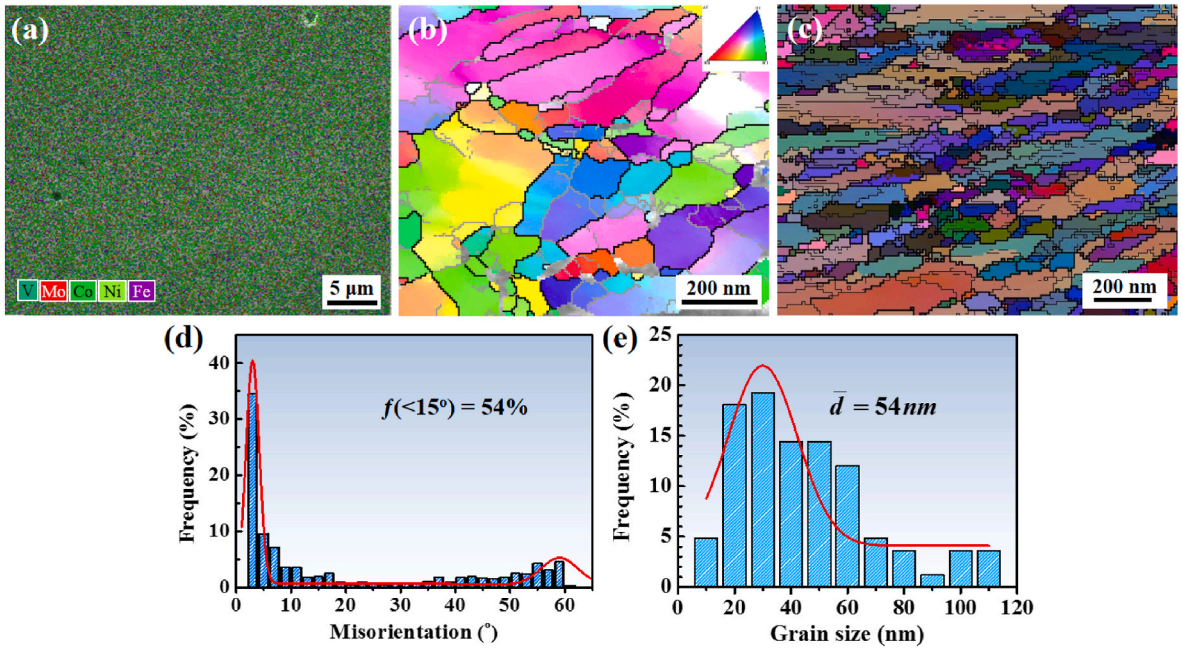

Fig. 3. EDS element distribution (a) and EBSD orientation imaging microscopy (OIM) images (b) (c) of the HPT processed FeNiCoMoV HEA, respectively. Black lines in (b) (c) indicate boundary misorientation >15°, and gray lines indicate misorientation between 2° and 15°. (d) The distribution of grain boundary misorientation angle. (e) Grain size distribution measured statistically from EBSD data.

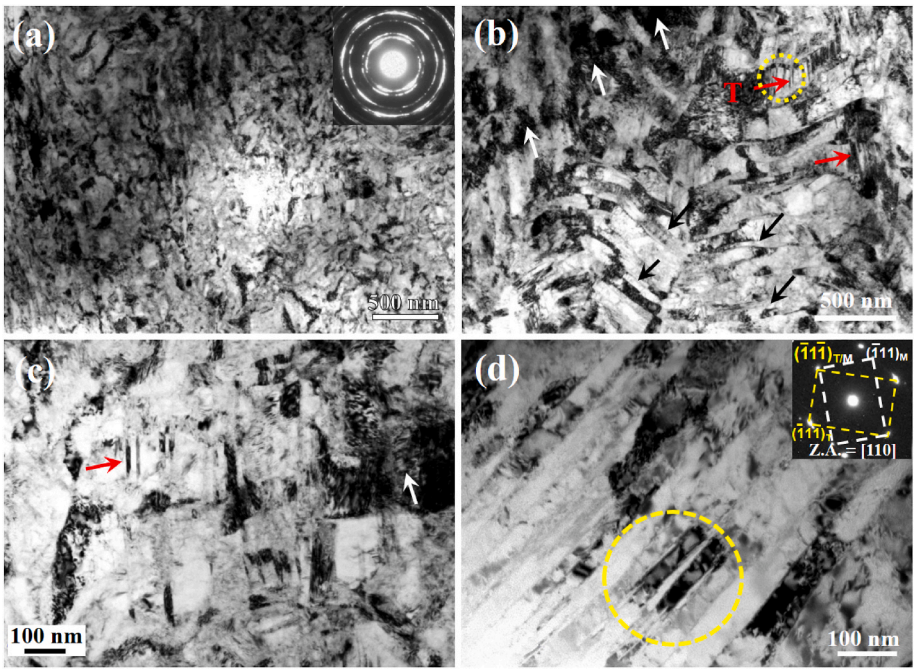

Fig. 4. Bright-field TEM micrographs taken from the edge region of the NC FeNi2CoMo0.2V0.5 HEA. (d) is the magnified image of yellow circled area in (b). Inset is the corresponding diffraction pattern, yellow circle indicates where SAED was made in (d). (For interpretation of the references to color in this figure legend, the reader is referred to the Web version of this article.)

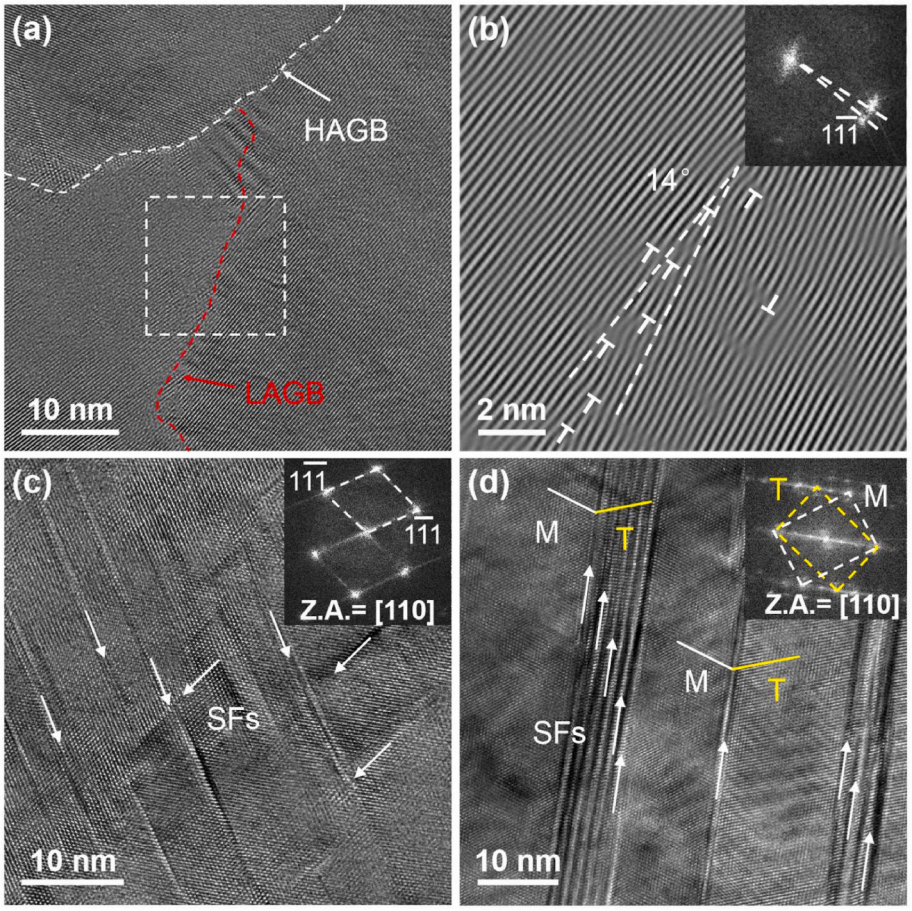

Fig. 5. HRTEM images taken from the disk edge of the HPT-processed FeNiCoMoV HEA. (a) HRTEM image showing a high angle GB (marked by the white dotted line) and a low angle GB (marked by the red dotted line). (b) (1-1-1) inverse filtered Fourier transformation (IFFT) image of the region (pointed out by the white rectangle) in (a) showing a 14° low angle GB. (c) [110] zone axis (Z.A.) HRTEM image showing the intersection microstructure of SFs (marked by the white arrows) at two {111} slip systems. (d) [110] zone axis (Z.A.) HRTEM image showing the twin lamellae (marked as "T") interspersed in the matrix ("M") and SFs (pointed out by white arrows). The corresponding FFT insets revealed the twin relationship. (For interpretation of the references to color in this figure legend, the reader is referred to the Web version of this article.)

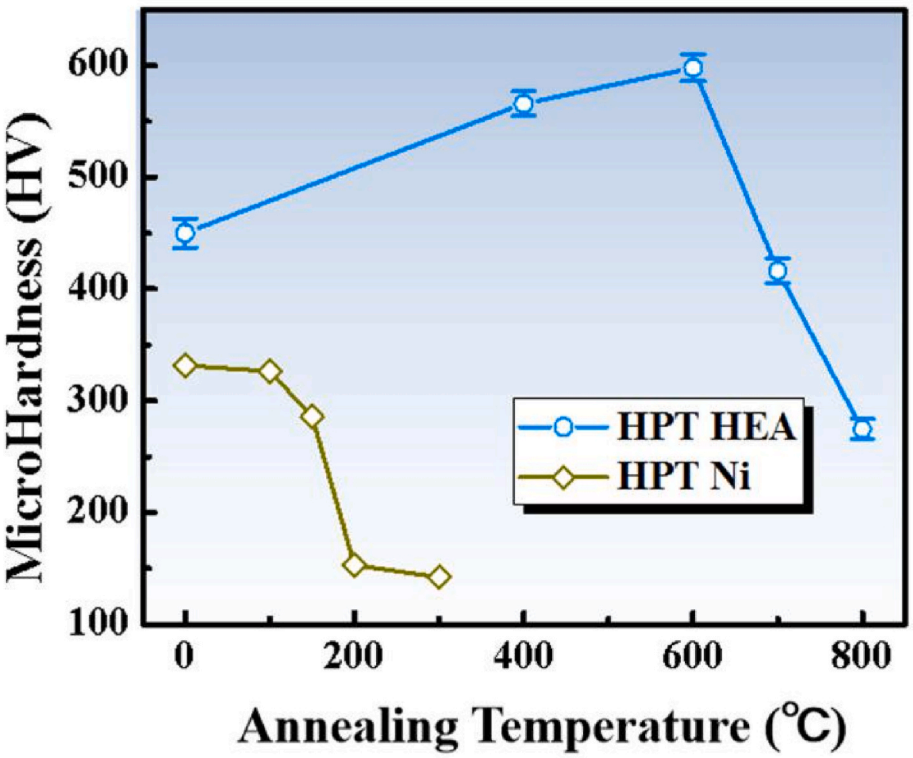

Fig. 6. Microhardness evolution during isochronally (1h) annealing for the HPT processed FeNiCoMoV HEA and pure Ni [46].

treatment for the NC FeNi2CoMo0.2V0.5 HEA comparing with NC Ni [45]. The microhardness rises from ~450 HV (the SPD state) to a maximum value of 600 HV at an annealing temperature of 600 °C, and then decreases to 270 HV at 800 °C. By contrast, the microhardness of the HPT processed pure Ni decreases sharply from 320 HV at 150 °C to 142 HV at 200 °C. The onset temperature (650 °C) of microhardness drop of the NC HEA is 500 °C higher than that of HPT processed pure Ni. The good thermal stability of the NC HEA derives from intrinsic high melting point and sluggish diffusion effect [13,15]. The main reason for annealing induced hardening (AIH) might be dislocation source-limited strengthening. GBs as dislocation source relaxed after annealing and higher force is needed to activate new deformations [46]. More comprehensive discussions are in section 4.

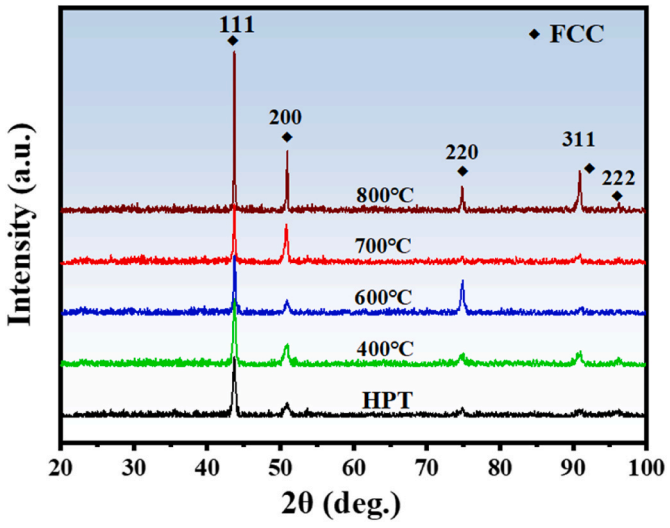

Fig. 7. XRD patterns of the HPT processed FeNiCoMoV HEA before and after annealing.

Fig. 7 illustrates the XRD patterns of HPT-produced FeNi2CoMo0.2V0.5 HEA before and after annealing. Only the single FCC phase was detected demonstrating that no obvious phase decomposition took place. Pronounced (111) and (200) peaks were detected before annealing, and the diffraction intensity of other peak positions is very small, indicating that notable texture or phenomenon preferred orientation occurs in the HEA after HPT deformation [31,47]. When the temperature was beyond 600 °C, (220) and (311) peaks became apparent showing that HPT and subsequent annealing have a significant effect on the texture components. The peak width decreased with rising temperatures, indicating grain coarsening and structural destabilization process. HPT induced apparent texture maintained at low temperatures, and faded away because of structure recovery, recrystallization induced grain orientation changes at high annealing temperatures [31].

Fig. 8 illustrates the microstructural evolutions of the HPT processed FeNi2CoMo0.2V0.5 HEA during isochronal annealing. Generally, with increasing temperature, recrystallized areas nucleate and grow, leading to a distribution (Fig. 8b) of new large grains coexist with deformed matrix [48–50]. At higher annealing temperature, the recrystallized grains gradually annex the deformed matrix via grain growth. As shown in Fig. 8a, most of the deformed NC grains were maintained when annealed at 600 °C. At the meantime, some grains recrystallized with average size of 1 μm. Recrystallization structure occupied most regions when the temperature rises to 700 °C (Fig. 8b) and coexisted with some small grains with a size of 200 nm. At 800 °C, the recrystallization was nearly completed with clean grains embedded with annealing twins (Fig. 8c). The recrystallized grains have an average size of 8 μm.

Fig. 9 displays TEM images after isochronal annealing of the HPT processed FeNi2CoMo0.2V0.5 HEA. As shown in Fig. 9a, the NC FeNi2CoMo0.2V0.5 HEA still kept an apparently NC/UFG microstructure when annealed at 400 °C. In addition, massive deformation twin lamellae were observed along with high-density dislocations accumulated within the twin-matrix lamellae, as shown in Fig. 9b. The corresponding HRTEM image in Fig. 10a shows nano-scale twin lamellae with

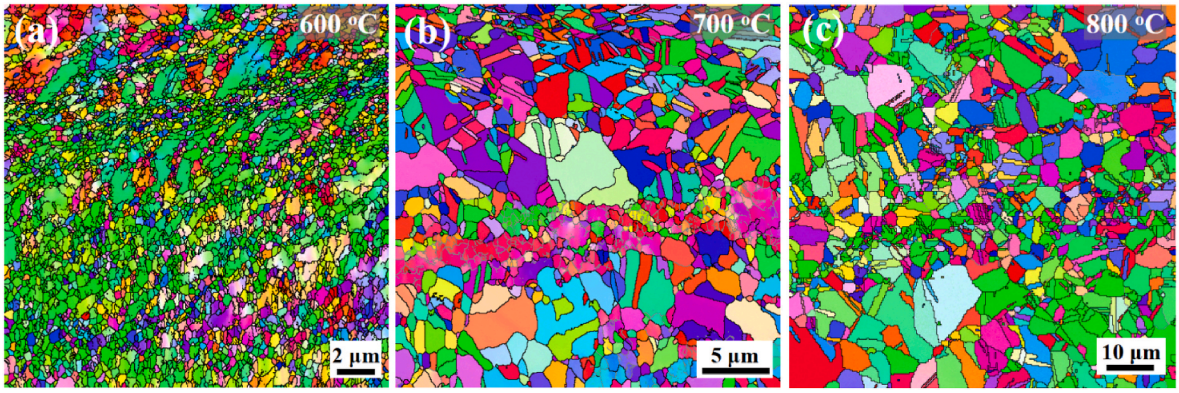

Fig. 8. OIM micrographs of the HPT processed FeNiCoMoV HEA during 1 h isochronal annealing at (a) 600 °C, (b) 700 °C, (c) 800 °C.

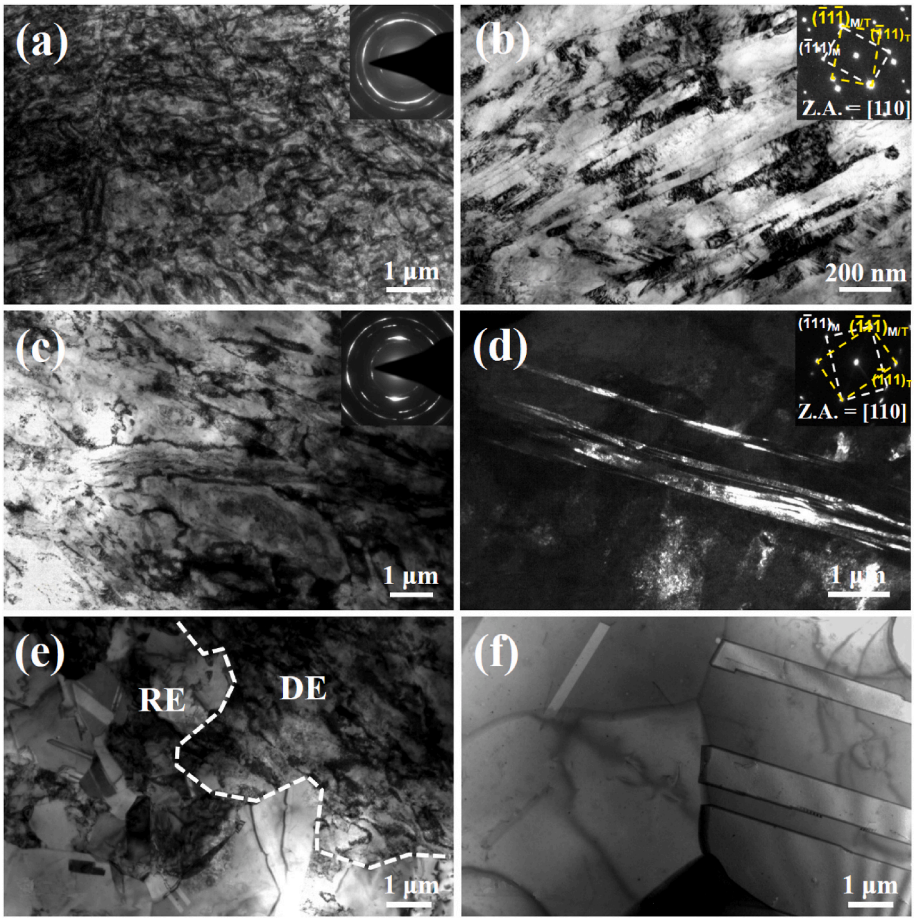

Fig. 9. Bright-field TEM images of the HPT processed FeNiCoMoV HEA samples isochronally annealed at 400 °C (a, b), 600 °C (c, d), 700 °C (e) and 800 °C (h). The area of deformed and recrystallized structure was labeled by "DE" and "RE" in (e), respectively.

rough TBs accompanying with massive SFs at TBs. With increasing the annealing temperature to 600 °C, the dislocation cell size remarkably increased, as shown in Fig. 9c, indicating a great decrement of dislocation density by recovery process. Moreover, a small amount of coarse deformation twin lamellae can be observed in Figs. 9d and 10b, resulting in a decrease of volume fraction of twin lamellae. After 700 °C annealing, only a small fraction of deformed structure was maintained in Fig. 9e and more than 50% of the area was recrystallized, resulting in a bimodal microstructure containing deformation region (marked as DE) and recrystallized (marked as RE), which agrees well with the EBSD results. A mass of annealing twins grown from GBs was observed inside recrystallized grains (Fig. 9e). The boundary of these growth twins was straight and aligned in the same direction within each individual grain. Most of the deformation twins have disappeared by structure recovery. With a further increase in annealing temperature to 800 °C (Fig. 9f), the recrystallization is almost complete and the grains and annealing twins become coarser. Moreover, as marked in Fig. 9f, annealing twins grew in two directions, parallel and perpendicular to the twin plane, resulting in a step-like twin boundary.

These observations again demonstrate the high thermal stability of the NC HEA. As seen from the whole annealing process, dislocation recovery occurs mainly before 600 °C, and the structure of dislocation cells

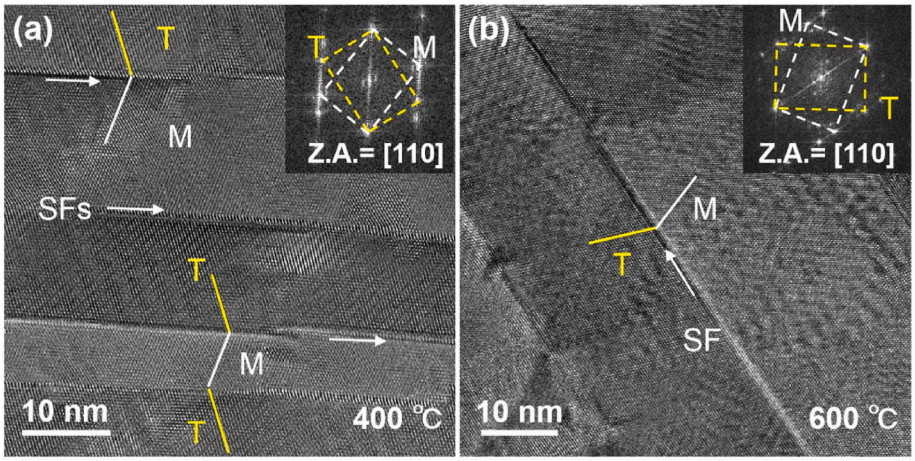

Fig. 10. [110] zone axis (Z.A.) HRTEM image showing the twin lamellae (marked as "T") interspersed in the matrix ("M") and SFs (pointed out by white arrows) of the annealed HPT HEA samples at 400 °C (a) and 600 °C (b) respectively. The corresponding FFT insets revealed the twin relationship.

remains. There is no precipitated phase during the whole recovery process. Good stability of the deformation twins resists thermal grain growth.

4. Discussion

4.1. Annealing induced hardening of FeNi2CoMo0.2V0.5 HEA

AIH was usually found in heavily deformed metallic materials especially at medium annealing temperatures [51], while softening was universal at higher temperatures derived from recrystallization and grain growth. Three mechanisms were summarized for AIH by a literate survey. One is the formation of special structure during annealing. Gu and Song [52] found abnormal hardening for cold-rolled CrMnFeCoNi HEA after subsequent annealing which resulted from the formation of long-range ordered structure in the HEA matrix. Annealing nanotwins in the HPT processed CoCrNi medium entropy alloy also contribute the AIH by the interaction with dislocations [53]. The second is the defects relaxation such as the annihilation of mobile dislocations inside the grains and their clustering into low energy configurations such as low-angle GBs [46,54]. In addition, the relaxation of non-equilibrium GBs also contributes to AIH since this relaxation leads to a more difficult emission of dislocations from the boundaries which was demonstrated in HPT processed CoCrNi medium entropy alloy [51,55]. The third, which is the most extensive mechanism, is the formation of second phase, precipitation and homologous multiphase structures [56]. Dislocations and boundaries could be pinned by these phase particles. Then recovery and boundary migration will be resisted which results in AIH. The above third reason was widely reported in HPT processed CrMnFeCoNi and TiZrNbHfTa alloy [12,57], cold-rolled Al-containing FeCoCrNiMn [58] and Refractory CoCrMoNbTi HEAs [59].

In present work, apparent AIH was observed for the HPT processed FeNi2CoMo0.2V0.5 HEA during medium isochronal annealing to 600 °C (Fig. 6). As examined by TEM, EDS and XRD scanning, no phase transformation, precipitation or second phase were detected after 600 °C treatment. As shown in Fig. 11a and Table 1, the density of geometrically necessary dislocations (GNDs) was calculated based on the EBSD data [60,61] as expressed in:

$$\rho_{GND} = \frac{2\theta_{KAM}}{Xb} \quad (1)$$

where θ_{KAM} is the kernel average misorientation (KAM), which is retrieved directly from EBSD data, X is kernel size, which is equal to twice the step size used in EBSD acquisition, b is the Burgers vector (b =

Table 1
EBSD parameters containing kernel average misorientation θ_{KAM}, step size, recrystallization fraction X_V, size of recrystallized grain D and calculated dislocation density ρ_{GND} for the HEA at different annealing conditions.

	θ_{KAM}	Step Size (nm)	ρ_{GND} (10^{17} m^{-2})	X_V	D (μm)
HPT	0.668	6	4.38		
400 °C	2.041	50	1.61		
600 °C	1.132	50	0.89	0.01	0.9
700 °C	0.389	50	0.31	0.6	3.5
800 °C				0.99	8.1

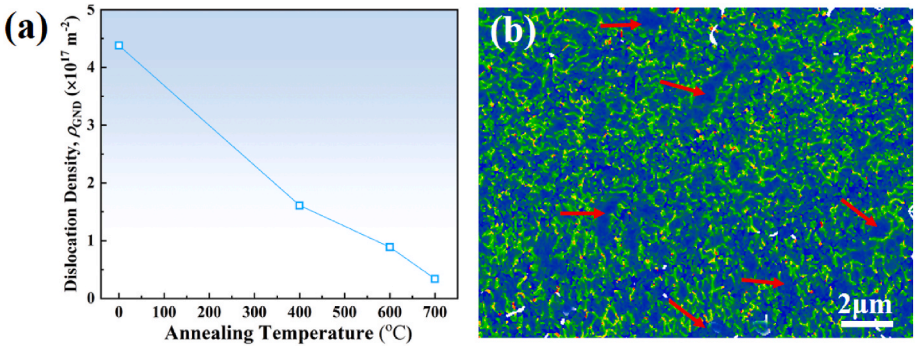

Fig. 11. (a) Density of GNDs of the as-processed and annealed HEA samples calculated based on EBSD data, (b) local misorientation map of the HEA sample annealed at 600 °C, blue, green and red colors in the rainbow bar represent low (<1°), medium (from 1° to 3°) and high (from 3° to 5°) misorientations, clean blue grains are marked by red arrows. (For interpretation of the references to color in this figure legend, the reader is referred to the Web version of this article.)

0.254 nm). The dislocation density decreased rapidly from 4.38 × 10^{17} m^{-2} at as-processed state to 1.6 × 10^{17} m^{-2} after 400 °C annealing, and then with moderate decrease to 0.89 × 10^{17} m^{-2} after 600 °C treatment. Only 0.31 × 10^{17} m^{-2} was maintained when annealed at 700 °C. Therefore, the annihilation of mobile dislocations and dislocation source made enormous contribution for AIH below 600 °C, as GNDs governing the flow stress of heat-treated samples [61]. This can be manifested by plenty of grains or regions with blue clean interior as shown in Fig. 11b. On the other hand, numerous deformation twin bundles were sustained when annealing below 600 °C. With dislocation densities decreasing, more room was empty out which is advantageous for the accumulation of newly generated dislocations and interaction with deformation twins. These results will lead to AIH.

4.2. Thermal stability of FeNi2CoMo0.2V0.5 HEA

4.2.1. Influence of activation energy on thermal stability

As reviewed on the evolution of microhardness (Fig. 6) and microstructure (Fig. 10), the HPT-processed FeNi2CoMo0.2V0.5 HEA performs an excellent thermal stability at the recrystallization temperature of 600–700 °C. The thermal stability is closely related to two processes of recrystallization and grain growth. Based on the classical Johnson–Mehl–Avrami–Kolmogorov (JMAK) model [3,62,63], the kinetics of static recrystallization was expressed as:

$$X_v = 1 - exp(-Bt^n) \tag{2}$$

where X_V is the fraction of recrystallization, t is the annealing time in seconds, B is a temperature-dependent parameter and n is the constant of JMAK exponent. As verified by Zi et al. [64], the recrystallized area fraction X_A could be used to replace X_V in Eq. (2) for the random distribution and isotropic shape of the recrystallized grains in the present case. Based on the Arrhenius law, B could be represented by:

$$B = B_0 \exp(-Q_r / RT) \tag{3}$$

where Q_r is the apparent activation energy of recrystallization (J/mol), T is absolute annealing temperature (K) and R is gas constant (8.314 J/(mol·K)). Then Eq. (2) can be expressed as:

$$\ln\left(\ln\frac{1}{1-X_A}\right) - n\ln t = \ln B_0 - \frac{Q_r}{RT} \tag{4}$$

The term ln[ln(1/1-X_A)] for isochronal annealing was plotted against $1/T$ by the recrystallization data at three different temperatures (600 °C, 700 °C and 800 °C) for the HPT processed alloy, as shown in Fig. 11a and listed in Table 1. Then the activation energy of recrystallization Q_r, can be calculated from the slope of the linear fitting lines to the data using the least square method, and it was determined to be ~350 kJ/mol.

The kinetics of recrystallization depends on the corresponding activation energy, which is related to elemental or lattice self-diffusion, and GB diffusion. At high enough temperatures, activation energy of recrystallization should be equal to the GB diffusion activation energy, which is usually proportional to the interatomic bonding force in the lattice [65]. In the current study, the activation energy of recrystallization was calculated to be 350 kJ/mol for lower temperatures, falls directly within the range of 300–400 kJ/mol for HEAs with elemental self-diffusion [50,65–67]. Meanwhile, the recrystallization activation energy here is much higher than that of steels, such as FeMnC alloy (~230 kJ/mol) [68], AISI 304LN stainless (150 kJ/mol) [69], TWIP steel (~229 kJ/mol) [70], suggesting sluggish element self-diffusion occurred during the annealing. The larger potential energy variation in lattice sites is responsible for higher activation energies for atom migration and decreased diffusion rates, resulting in sluggish diffusion in HEAs. The lack of a major diffusion element and a huge discrepancy of atoms size also weighted in favor of sluggish diffusion.

The inexistence of precipitates conduced rapid grain migration and microstructure coarsening during annealing. Then apparent grain growth was observed for the recrystallized area compared with the as-HPT processed alloy. The grain growth kinetics can be evaluated using the classical theory described by Eq. (5) [50,65], where D is the instantaneous grain size at a given annealing time (μm), D_0 is the initial grain size (μm), n is the grain growth exponent, t is the annealing time (s), and k is a kinetic constant controlling the diffusion process at a specific temperature.

$$D^n - D_0^n = kt \tag{5}$$

Since annealing was performed on the deformed alloy, the initial grain size (D_0) can be assumed approximately equal to zero [71] and the power-law can be simplified:

$$D^n = kt \tag{6}$$

A grain growth exponent $n \sim 3$ can be easily obtained from the slope of the ln$D$ vs ln$t$ plot. The kinetics constant k in Eq. (4) can be expressed in Arrhenius form and Eq. (6) was rewritten in:

$$D^n / t = k_0 \exp(-Q_g / RT) \tag{7}$$

where Q_g is the activation energy for grain growth, k_0 is a constant and T is the absolute annealing temperature. As shown in Fig. 12b, the activation energy for grain growth was calculated as $Q_g = 272$ kJ/mol from the slope of the $1/T$ vs ln (D^n/t), as shown in Table 1.

The activation energy of grain growth was lower than that of recrystallization, indicating a swift GB migration process and a slow defects recovery process of recrystallization. The retardation of recrystallization is attributed to the sluggish diffusion effect at lower temperatures as revealed earlier. Moreover, a mass of deformation twins (shown in Fig. 10) also intercepted dislocations as barriers, contributing to a tough recrystallization process.

4.2.2. Influence of TB on thermal stability

For the HPT-processed FeNi2CoMo0.2V0.5 HEA, the high-density twin lamellae provide an effective approach for achieving thermal stability in fine-grained systems. The enhanced thermal stability of twinned microstructure can be understood by considering the role of TBs in reducing the migration rate of GBs, by lowering the overall coarsening rate. On the one hand, the coherent TB is well known to be immobile in response to thermal agitation. This is the high order in the TB plane imposed restricted diffusion of impurities. On the other hand, the TB energy is two orders of magnitude smaller than the ordinary grain boundary [26,72]. The driving force for reducing the total GB energy of the system via grain coarsening is obviously higher than that for the reduction of twin boundary energy. Consequently, the stability observed in the HPT-processed FeNi2CoMo0.2V0.5 HEA sample may then at least partially be attributed to the high density of coherent TBs.

Expect the single TBs, the TB-GB triple junctions (TJs) formed by the intersection of high coincident site lattice (CSL) boundaries, also play an important role for the thermal stability. The TJs with finite mobility hindered boundary migration The direct observations and molecular dynamics (MD) simulations of boundary migration [24], suggest that TB-GB TJs limit coarsening by imposing a drag effect on GB migration. Recent in situ observations of GB migration by kink motion and ledge growth in nano-twinned copper have indicated that kink motion is stagnated at TB-GB TJs, where a low nucleation rate of kinks and ledges arose at TJ [73]. The more compact atomic arrangement of the TB-GB TJ presents a significant energy barrier to kink nucleation, whereas open boundary and junction structures can be envisaged to have a smaller barrier. Thus, considering the high density of twin lamellae in HPT-processed FeNi2CoMo0.2V0.5 HEA, the observed stability could certainly be a consequence of low kink nucleation rates that hinder thermally activated GB motion.

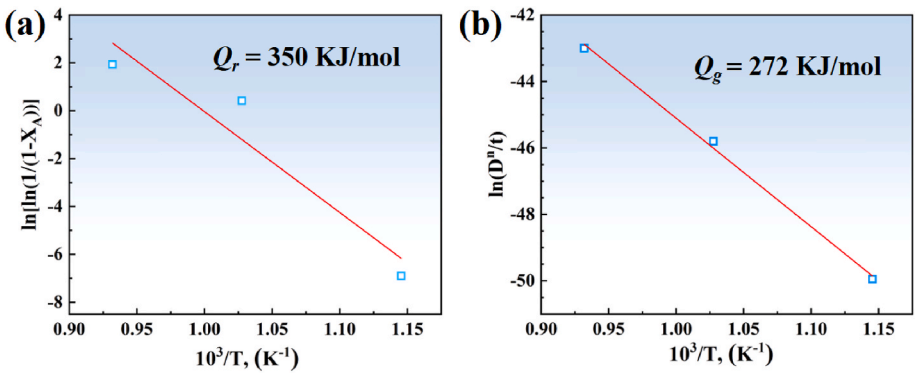

Fig. 12. Arrhenius plot of ln[ln(1/1-X_A)] vs 1/T (a) and ln (D^n/t) vs 1/T (b) derived from the kinetics of recrystallization and grain growth for HPT processed HEA annealed at 600, 700 and 800 °C.

5. Conclusions

In summary, FeNi2CoMo0.2V0.5 HEA was prepared by HPT and isothermal annealing treatment, and the evolution of microstructure was investigated meticulously by XRD, EBSD and TEM analyses. Kinetic measurements of activation energy during annealing were carried out to understand the thermal stability. The following conclusions can be made.

(1) Nano-scaled grains and deformation twins were obtained after HPT at edge region with a hardness plateau of 450 HV. From edge to the center, the hardness decreased gradually and dislocation cells and ordered dislocations were observed.
(2) After annealing at lower temperatures below 600 °C, a distinct AIH was performed from 450 HV to 600 HV, resulting from annihilation of mobile dislocations and interaction with deformation twins without precipitation effect.
(3) The activation energy of recrystallization was calculated to be 350 kJ/mol which is higher than that of grain growth (272 kJ/mol). Sluggish diffusion effect and deformation twin lamellae retarded the movement of dislocations and GB overcoming structure reconstruction induced high thermal stability of HPT processed FeNi2CoMo0.2V0.5 HEA.
(4) Deformation twin induced high thermal stability of HPT-processed FeNi2CoMo0.2V0.5 HEA by immobility and lower TB energy. TB-GB triple junctions stagnated kink motion and kink nucleation also contributed to the thermal stability.

Data availability statement

The raw/processed data required to reproduce these findings cannot be shared at this time as the data also forms part of an ongoing study.

CRediT authorship contribution statement

N.N. Liang: Conceptualization, Data curation, Writing – original draft. **R.R. Xu:** Funding acquisition, Supervision. **G.Z. Wu:** Investigation, Data curation. **X.Z. Gao:** Investigation, Data curation. **Y.H. Zhao:** Writing – review & editing, Funding acquisition, Supervision.

Declaration of competing interest

The authors declare that they have no known competing financial interests or personal relationships that could have appeared to influence the work reported in this paper.

Acknowledgments

The authors would like to acknowledge financial supports from Natural Science Foundation of Jiangsu Province (Grant No. BK20190478), the National Key R&D Program of China (Grant No. 2017YFA0204403), National Natural Science Foundation of China (Grant No. 52105368, 51931003, 51971112and 51225102) and the Fundamental Research Funds for the Central Universities (Grant No. 30919011405). The authors are thankful for the technical support from Jiangsu Key Laboratory of Advanced Micro&Nano Materials and Technology, and the Materials Characterization Facility of Nanjing University of Science and Technology.

References

[1] X.Y. Li, Z.H. Jin, X. Zhou, K. Lu, Science 370 (2020) 831–836.
[2] Y. Huang, S. Sabbaghianrad, A.I. Almazrouee, K.J. Al-Fadhalah, S.N. Alhajeri, T. G. Langdon, Mat. Sci. Eng. Struct. 656 (2016) 55–66.
[3] N.N. Liang, Y.H. Zhao, Y. Li, T. Topping, Y.T. Zhu, R.Z. Valiev, E.J. Lavernia, J. Mater. Sci. 53 (2018) 13173–13185.
[4] X.Y. Song, J.X. Zhang, L.M. Li, K.Y. Yang, G.Q. Liu, Acta Mater. 54 (2006) 5541–5550.
[5] C.C. Koch, R.O. Scattergood, K.A. Darling, J.E. Semones, J. Mater. Sci. 43 (2008) 7264–7272.
[6] J. Hu, Y.N. Shi, K. Lu, Scripta Mater. 154 (2018) 182–185.
[7] F. Abdeljawad, S.M. Foiles, Acta Mater. 101 (2015) 159–171.
[8] N.N. Liang, J.Z. Liu, S.C. Lin, Y. Wang, J.T. Wang, Y.H. Zhao, Y.T. Zhu, J. Alloys Compd. 735 (2018) 1389–1394.
[9] Y. Zhang, T.T. Zuo, Z. Tang, M.C. Gao, K.A. Dahmen, P.K. Liaw, Z.P. Lu, Prog. Mater. Sci. 61 (2014) 1–93.
[10] M.J.R. Haché, C. Cheng, Y. Zou, J. Mater. Res. 35 (2020) 1051–1075.
[11] F. Otto, A. Dlouhy, C. Somsen, H. Bei, G. Eggeler, E.P. George, Acta Mater. 61 (2013) 5743–5755.
[12] B. Schuh, F. Mendez-Martin, B. Volker, E.P. George, H. Clemens, R. Pippan, A. Hohenwarter, Acta Mater. 96 (2015) 258–268.
[13] K.Y. Tsai, M.H. Tsai, J.W. Yeh, Acta Mater. 61 (2013) 4887–4897.
[14] Z.Z. Li, S.T. Zhao, R.O. Ritchie, M.A. Meyers, Prog. Mater. Sci. 102 (2019) 296–345.
[15] N.X. Zhou, T. Hu, J.J. Huang, J. Luo, Scripta Mater. 124 (2016) 160–163.
[16] H.W. Deng, Z.M. Xie, M.M. Wang, Y. Chen, R. Liu, J.F. Yang, T. Zhang, X.P. Wang, Q.F. Fang, C.S. Liu, Y. Xiong, Mat. Sci. Eng. Struct. 774 (2020), 138925.
[17] C.-Y. Cheng, J.-W. Yeh, Mater. Lett. 181 (2016) 223–226.
[18] S. Praveen, J. Basu, S. Kashyap, R.S. Kottada, J. Alloys Compd. 662 (2016) 361–367.
[19] Y.Y. Zhao, H.W. Chen, Z.P. Lu, T.G. Nieh, Acta Mater. 147 (2018) 184–194.
[20] D.B. Miracle, O.N. Senkov, Acta Mater. 122 (2017) 448–511.
[21] O.N. Senkov, G.B. Wilks, D.B. Miracle, C.P. Chuang, P.K. Liaw, Intermetallics 18 (2010) 1758–1765.
[22] Y. Zou, H. Ma, R. Spolenak, Nat. Commun. 6 (2015) 7748.
[23] X. Zhang, A. Misra, Scripta Mater. 66 (2012) 860–865.
[24] C. Saldana, T.G. Murthy, M.R. Shankar, E.A. Stach, S. Chandrasekar, Appl. Phys. Lett. 94 (2009) 21910.
[25] K. Lu, Nat. Rev. Mater. 1 (2016), 16019.
[26] X. Zhang, A. Misra, H. Wang, J.G. Swadener, A.L. Lima, M.F. Hundley, R. G. Hoagland, Appl. Phys. Lett. 87 (2005), 233116.
[27] C. Saldana, A.H. King, E.A. Stach, W.D. Compton, S. Chandrasekar, Appl. Phys. Lett. 99 (2011), 231911.
[28] X. Zhou, X. Li, K. Lu, Phys. Rev. Lett. 122 (2019), 126101.
[29] N. Liang, X. Wang, Y. Cao, Y. Li, Y. Zhu, Y. Zhao, Entropy 22 (2020) 1074.

[30] Y.H. Zhao, X.Z. Liao, Y.T. Zhu, Z. Horita, T.G. Langdon, Mat. Sci. Eng. Struct. 410 (2005) 188–193.
[31] H. Shahmir, J. He, Z. Lu, M. Kawasaki, T.G. Langdon, Mater. Sci. Eng. A 676 (2016) 294–303.
[32] H. Shahmir, M. Nili-Ahmadabadi, A. Shafiee, M. Andrzejczuk, M. Lewandowska, T. G. Langdon, Mat. Sci. Eng. Struct. 725 (2018) 196–206.
[33] A.P. Zhilyaev, T.G. Langdon, Prog. Mater. Sci. 53 (2008) 893–979.
[34] R. Sonkusare, K. Biswas, N. Al-Hamdany, H.G. Brokmeier, R. Kalsar, N. Schell, N. P. Gurao, Mat. Sci. Eng. Struct. 782 (2020), 139187.
[35] D.H. Lee, I.C. Choi, G.H. Yang, Z.P. Lu, M. Kawasaki, U. Ramamurty, R. Schwaiger, J.I. Jang, Scripta Mater. 156 (2018) 129–133.
[36] H. Shahmir, T. Mousavi, J.Y. He, Z.P. Lu, M. Kawasaki, T.G. Langdon, Mat. Sci. Eng. Struct. 705 (2017) 411–419.
[37] L. Jiang, Y.P. Lu, M. Song, C. Lu, K. Sun, Z.Q. Cao, T.M. Wang, F. Gao, L.M. Wang, Scripta Mater. 165 (2019) 128–133.
[38] P.F. Yu, H. Cheng, L.J. Zhang, H. Zhang, Q. Jing, M.Z. Ma, P.K. Liaw, G. Li, R.P. Liu, Mat. Sci. Eng. Struct. 655 (2016) 283–291.
[39] J.B. Liu, C.X. Chen, Y.Q. Xu, S.W. Wu, G. Wang, H.T. Wang, Y.T. Fang, L. Meng, Scripta Mater. 137 (2017) 9–12.
[40] Y. Li, Y.H. Zhao, W. Liu, C. Xu, Z. Horita, X.Z. Liao, Y.T. Zhu, T.G. Langdon, E. J. Lavernia, Mater. Sci. Eng. A 527 (2010) 3942–3948.
[41] Z.J. Zhang, Q.Q. Duan, X.H. An, S.D. Wu, G. Yang, Z.F. Zhang, Mater. Sci. Eng. A 528 (2011) 4259–4267.
[42] S. Scheriau, Z. Zhang, S. Kleber, R. Pippan, Mat. Sci. Eng. Struct. 528 (2011) 2776–2786.
[43] Y.P. Li, S. Wu, H.K. Bian, N. Tang, B. Liu, Y. Koizumi, A. Chiba, Scripta Mater. 68 (2013) 171–174.
[44] W. Wu, M. Song, S. Ni, J. Wang, Y. Liu, B. Liu, X. Liao, Sci. Rep. 7 (2017) 46720.
[45] H.W. Zhang, X. Huang, R. Pippan, N. Hansen, Acta Mater. 58 (2010) 1698–1707.
[46] X. Huang, N. Hansen, N. Tsuji, Science 312 (2006) 249–251.
[47] Z.Y. Li, L.M. Fu, H. Zheng, R. Yu, L.F. Lv, Y.L. Sun, X.P. Dong, A.D. Shan, Metall. Mater. Trans. 50A (2019) 3223–3237.
[48] O.F. Higuera-Cobos, J.M. Cabrera, Mater. Sci. Eng. A 571 (2013) 103–114.
[49] G. Laplanche, O. Horst, F. Otto, G. Eggeler, E.P. George, J. Alloys Compd. 647 (2015) 548–557.
[50] M. Annasamy, N. Haghdadi, A. Taylor, P. Hodgson, D. Fabijanic, Mat. Sci. Eng. Struct. 754 (2019) 282–294.
[51] J. Gubicza, Adv. Eng. Mater. 22 (2020), 1900507.
[52] J. Gu, M. Song, Scripta Mater. 162 (2019) 345–349.
[53] H.W. Deng, Z.M. Xie, B.L. Zhao, Y.K. Wang, M.M. Wang, J.F. Yang, T. Zhang, Y. Xiong, X.P. Wang, Q.F. Fang, C.S. Liu, Mat. Sci. Eng. Struct. 744 (2019) 241–246.
[54] X.Y. Zhang, Q. Liu, X.L. Wu, A.W. Zhu, Appl. Phys. Lett. 93 (2008), 261907.
[55] S. Praveen, J.W. Bae, P. Asghari-Rad, J.M. Park, H.S. Kim, Mat. Sci. Eng. Struct. 734 (2018) 338–340.
[56] L.X. Sun, N.R. Tao, M. Kuntz, J.Q. Yu, K. Lu, J. Mater. Sci. Technol. 30 (2014) 731–735.
[57] B. Schuh, B. Volker, J. Todt, N. Schell, L. Perriere, J. Li, J.P. Couzinie, A. Hohenwarter, Acta Mater. 142 (2018) 201–212.
[58] Z.Y. Li, L.M. Fu, J. Peng, H. Zheng, A.D. Shan, Mat. Sci. Eng. Struct. 786 (2020), 139446.
[59] M.N. Zhang, X.L. Zhou, W.Z. Zhu, J.H. Li, Metall. Mater. Trans. 49A (2018) 1313–1327.
[60] M. Calcagnotto, D. Ponge, E. Demir, D. Raabe, Mat. Sci. Eng. Struct. 527 (2010) 2738–2746.
[61] Y. Liu, Y. Cao, Q. Mao, H. Zhou, Y. Zhao, W. Jiang, Y. Liu, J.T. Wang, Z. You, Y. Zhu, Acta Mater. 189 (2020) 129–144.
[62] Y.H. Zhao, T. Topping, Y. Li, E.J. Lavernia, Adv. Eng. Mater. 13 (2011) 865–871.
[63] Y.L. Wang, R. Lapovok, J.T. Wang, Y.S. Qi, Y. Estrin, Mater. Sci. Eng. A 628 (2015) 21–29.
[64] A. Zi, I. Stulikova, B. Smola, Mat. Sci. Eng. Struct. 527 (2010) 1469–1472.
[65] G.W. Hu, L.C. Zeng, H. Du, X.W. Liu, Y. Wu, P. Gong, Z.T. Fan, Q. Hu, E.P. George, J. Mater. Sci. Technol. 54 (2020) 196–205.
[66] W.H. Liu, Y. Wu, J.Y. He, T.G. Nieh, Z.P. Lu, Scripta Mater. 68 (2013) 526–529.
[67] M.H. Mohammad-Ebrahimi, A. Zarei-Hanzaki, H.R. Abedi, S.M. Vakili, C. K. Soundararajan, J. Alloys Compd. 806 (2019) 1550–1563.
[68] Y. Lü, D.A. Molodov, G. Gottstein, Acta Mater. 59 (2011) 3229–3243.
[69] R. Singh, G. Das, P.K. Singh, I. Chattoraj, Metall. Mater. Trans. 40A (2009) 1219–1234.
[70] F. de las Cuevas, M. Reis, A. Ferraiuolo, G. Pratolongo, L.P. Karjalainen, V. García Navas, J. Gil Sevillano, Adv. Mater. Res. 89–91 (2010) 153–158.
[71] Z. Wu, H. Bei, F. Otto, G.M. Pharr, E.P. George, Intermetallics 46 (2014) 131–140.
[72] L.X. Sun, N.R. Tao, K. Lu, Scripta Mater. 99 (2015) 73–76.
[73] K.C. Chen, W.W. Wu, C.N. Liao, L.J. Chen, K.N. Tu, Science 321 (2008) 1066–1069.